nature reviews physics

https://doi.org/10.1038/s42254-024-00766-5

Perspective

Check for updates

The physics of freezing and melting in the presence of flows

Yihong Du[1], Enrico Calzavarini[2] & Chao Sun[1,3]

Abstract

Ice in the environment plays a central role in both global-scale processes on Earth and many human activities. Issues related to its description, including the modelling of natural ice dynamics from the smallest to the largest scales, are of great importance. In the natural environment, melting or freezing processes are typically coupled to those of fluid flows. Therefore, the interplay between fluid mechanics and phase-change thermodynamics is a highly topical problem. In recent years, fluid–ice interface problems have been studied via not only field measurements but also laboratory experiments, numerical simulations and theoretical analyses. This Perspective considers the state-of-the-art knowledge of the phenomenology of fluid–ice coupling processes in standardized configurations. These include freezing and melting in thermally stratified natural convection of fresh water, double-diffusive convection and convection in the mushy ice of salty water in confined systems, as well as imposed flows moving along an ice layer or surrounding dispersed ice bodies. It also highlights open questions of geophysical interest that could benefit from fundamental studies with a physical and fluid dynamic approach.

Sections

[1]New Cornerstone Science Laboratory, Center for Combustion Energy, Key Laboratory for Thermal Science and Power Engineering of MoE, Department of Energy and Power Engineering, Tsinghua University, Beijing, China. [2]Université de Lille, Unité de Mécanique de Lille — J. Boussinesq (UML), Lille, France. [3]Department of Engineering Mechanics, School of Aerospace Engineering, Tsinghua University, Beijing, China. e-mail: chaosun@tsinghua.edu.cn

Introduction

Ice, covering nearly one-tenth of Earth's surface, forms and melts in response to changing environmental conditions. It is an important component of many geophysical processes on timescales ranging from hours to seasons, years and even geological ages[1–5]. Its evolution plays a crucial role in the global water cycle and global climate, influencing the sea level[6–8], ocean circulation[6,9,10], ocean surface temperature[9,10] and land-surface albedo[9,11,12]. The current global decline of ice[13] is already having important biological consequences[14]. Examples include alterations in ecological niches, biodiversity[15] and ocean productivity[16,17], impact on the global carbon cycle[18], and release of pathogens and microplastics into the oceans[19–21]. In addition, landforms and other geological patterns are shaped by the growth and melting of ice[22]. Ice is also a valuable freshwater resource[23], and in high-latitude and polar regions it has a strong effect on human activities such as navigation and the fishery industry[24,25].

The physics of freezing and melting has been extensively explored since the early work by Josef Stefan on the diffusive advance of a freezing front[26–28]. In most natural cases, however, ice interacts with fluid flows in the surrounding environment[29–32]. The coupling of fluid mechanics and phase change is nowadays explored in laboratory studies. Such studies benefit from the rapid development of experimental, numerical and theoretical methods (Box 1). The connection with geophysical-scale processes is then performed by invoking scaling analysis and by means of a vast set of dimensionless numbers characterizing the scales (Table 1).

Freezing and melting typically involve spatial temperature variations, which cause a gravity-induced buoyancy force and set the liquid into motion. This makes buoyancy-driven thermal convection, also known as natural convection, one of the most common types of flow coupled with phase change. An idealized model system for natural convection is the Rayleigh–Bénard convection (RB) system, a fluid layer typically enclosed in a cubic or cylindrical container heated from below and cooled from above. In such conditions, most fluids (with the notable exception of water, as discussed below) are unstably stratified. In this system, as the fluid at the bottom heats up and becomes less dense, buoyant forces push it upward toward the cooler part of the container. Meanwhile, the denser, cooler fluid at the top sinks, displacing the warmer fluid below. This process drives a cyclical motion, forming convection rolls between the two boundaries. This closed system is very attractive for laboratory research because of its high degree of controllability. Many of its dynamical properties, in regimes from the onset of convection to the ultimate regime of turbulent convection, have been characterized in great detail[33–37]. Some other typical configurations are realized when the RB system is tilted, notably by 90° (vertical convection, VC)[38,39], or flipped (flipped Rayleigh–Bénard convection, FRB). The detailed knowledge of fluid dynamic processes in these systems makes them perfect candidates

Box 1 | Common methods in laboratory studies on freezing and melting in the presence of flows

Experimental approaches

Improved controllability and the use of advanced flow visualization and measurement techniques have greatly expanded the applicability of experiments. Some common techniques are as follows.

- **Schlieren, shadowgraph and interferometry techniques** are based on the refraction of light as it passes through an inhomogeneous fluid. Changes in the density (temperature, concentration) field are converted into light intensity and can thus be measured.
- **Particle image velocimetry** can measure the velocity field based on the correlation of tracer particle images photographed over a very short time interval.
- **Laser Doppler anemometry** can measure the velocity at a specific location based on the frequency shift of light scattered by tracer particles (Doppler effect).

Numerical approaches

Several methods have been developed to deal with phase change at the solid–liquid interface. In numerical simulations, inaccuracies can result from simplifications and assumptions — for example ignoring the density difference between solid and liquid, adopting the Boussinesq approximation (which assumes constant density except for that in the buoyancy term) or assuming a diffusive interface. However, multiphase numerical simulation can generally provide rich and reliable information on the behaviours of the system.

- **The phase-field method** treats the solid–liquid interface as a diffusive interface by introducing a phase-field variable. This allows the same set of equations to be solved for the entire computational domain.
- **The enthalpy method** solves the enthalpy distribution with a unified energy equation over the entire domain to determine the interface and the temperature distribution. This method also introduces a thickness for a smooth solid–fluid interface.
- **The immersed boundary method** treats the solid–fluid interface by applying localized volumetric forces.

Theoretical approaches

Some theoretical tools commonly used to predict the scaling relations among various properties are as follows.

- **Scaling analysis** is a technique used to understand how different physical quantities change with the properties of the system or with different flow conditions, which helps to simplify complex problems by identifying the dominant factors and relevant dimensionless numbers. It includes force balance and energy budget analysis, dimensional analysis, the similarity principle and other methods in fluid dynamics.
- **Stability analysis** examines how the perturbation amplitude varies with time after a small perturbation is introduced into the system. It is commonly used to predict the interfacial dynamics and to analyse the onset conditions of flow instability.
- **Boundary-layer theory** states that viscosity effect dominates in a thin region close to the solid phase for high-Reynolds-number flows (see Table 1 for the definition of the Reynolds number).

for studying phase-change processes and their coupling with fluid flows. The most commonly used paradigm is the classical RB system, and its variations as VC and FRB, with the addition of a melting or freezing boundary.

Early experiments on liquid freezing from above demonstrated the effect of convective flows on the dynamics and morphology of the ice front[40]. Such couplings between flow and phase change have also been examined in detail using multiphase numerical simulations. In pure liquids, the typical advection timescale of the flow is much faster than that associated with the phase change. As a consequence, the flow dynamics of the system are strikingly similar to those of the single-phase (that is, fluid-only) RB system and the interface evolution is closely tied to that of the fluid flow[41–43]. As important coherent structures in the system, plumes serve as the main heat carriers. Hot plumes detached from the bottom surface impact on the ice front, whereas the cold plumes ejected from the ice front move towards to the bottom surface. The heat-flux difference between the plume ejection regions and plume impact regions leads to an uneven ice front morphology[44], which is rougher if the buoyant forcing is stronger[41]. Furthermore, in certain parameter regimes, bistable states can occur. The system establishes either a diffusive or a convective equilibrium, depending on the initial setup conditions[45].

When considering ice in lakes, rivers and oceans, many other types of fluid flow and physical coupling are relevant (Fig. 1a,b). In this Perspective, we focus on the stratified convection in fresh water, double-diffusive convection in salty water, brine convection in mushy ice, and externally forced flows that are adjacent to ice layers or impact dispersed ice bodies. By reviewing recent laboratory results, we aim to reveal the intricate interaction mechanisms between fluid dynamics, heat and mass transfer, and solid–liquid phase-change processes. We also aim to highlight potential future research directions for the physics and fluid mechanics community to improve the quantitative description of ice and sea-ice melting in the current global warming era. We first review the role of stratified convection in freezing and melting in fresh water (Fig. 1c). We then move on to the effects of double-diffusive convection (Fig. 1d) and convection within mushy ice (Fig. 1e), both of which are typical of freezing and melting in salty water. Next, we focus on the situation where ice, either extended as a system boundary (Fig. 1f) or having a limited spatial size (Fig. 1g), is subject to external flows. After that, we discuss the implications of these fluid dynamic processes for phenomena in the natural world (cryosphere and hydrosphere). Finally, we offer our outlook on currently open issues that may be useful to guide research in the coming years.

Table 1 | Important dimensionless numbers in the coupled physics of phase change and fluid flow

Dimensionless number	Definition	Physical meaning
Lewis number	$Le=\alpha/D$	Ratio of thermal diffusivity to mass diffusivity
Nusselt number	$Nu=QH/(\lambda\Delta T)$	Ratio of convective heat transfer to diffusive heat transfer
Péclet number	$Pe=UH/\alpha$	Ratio of convection to thermal diffusion
Prandtl number	$Pr=\nu/\alpha$	Ratio of kinetic viscosity to thermal diffusivity
Rayleigh number	$Ra=g\Delta\rho^{*}H^{3}/(\nu\alpha)$	Ratio of destabilizing buoyancy to diffusive resistance
Rayleigh–Darcy number	$Ra_D=Kg\Delta\rho^{*}H/(\nu\alpha)$	Ratio of buoyancy to diffusive resistance in porous media
Reynolds number	$Re=UH/\nu$	Ratio of inertial forces to viscous forces
Richardson number	$Ri=g\Delta\rho^{*}H/U^{2}$	Ratio of buoyancy to shear
Schmidt number	$Sc=\nu/D$	Ratio of kinetic viscosity to mass diffusivity
Sherwood number	$Sh=JH/(D\Delta C)$	Ratio of convective mass transfer to diffusive mass transfer
Stefan number	$Ste=L/(C_p\Delta T)$	Ratio of latent heat to sensible heat

α, thermal diffusivity; ΔC, concentration difference; $\Delta\rho^{*}$, dimensionless density difference; ΔT, temperature difference; λ, thermal conductivity; ν, kinetic viscosity; C_p, heat capacity of the solid; D, mass diffusivity; g, gravitational acceleration; H, length scale; J, mass flux; K, Darcy permeability coefficient; L, latent heat; Q, heat flux; U, velocity.

Freezing and melting in thermally stratified fresh water

Water has unique chemical and physical properties. In its liquid phase, it shows a rare inversion of thermal expansion coefficient: the density of pure water at atmospheric pressure reaches an absolute maximum at about 4 °C (density-peak temperature) (Fig. 1c). As a result, above the density-peak temperature, water is positively buoyant (hot water is lighter than cold water), whereas water between the freezing point (~0 °C) and the density-peak temperature experiences a reversed buoyancy force (water is lighter approaching the freezing temperature; ice floats on water). This fact is responsible for intricate nonlinear and non-monotonous phenomena in the freezing and melting of thermally stratified water layers.

The morphology of a melting ice block in a water tank varies greatly in laboratory experiments, depending on the ambient temperature (Fig. 2a–c). As revealed by experiments and simulations, when the ambient water is at 4 °C, the water near the ice block flows upwards because it is lighter than ambient water, creating a downward ice pinnacle (Fig. 2a,d). Conversely in an 8 °C environment, the water near the ice block is overall denser as the mass fraction of water in the 4–8 °C temperature interval is larger than that in the 0–4 °C range. The resulting downward water motion shapes an upward pinnacle (Fig. 2c,f). Interestingly, at an intermediate ambient temperature of 5.6 °C, the upward flow near the ice–water interface and the downward flow at about 4 °C are of comparable intensity. Therefore, convective rolls develop in the water region between 0 and 4 °C and shape scallop patterns on the ice front[46] (Fig. 2b,e). Likewise, the upward convective current (reversed-buoyant flow) of water between 0 and 4 °C plays a dominant role in shaping the lateral ice front in VC systems[47,48].

Fluid convection coupled to phase change is also affected by the water density anomaly when the temperature gradient is in the vertical direction, as in the RB configuration. In such circumstances, whether the water layers are gravitationally stable or unstable depends on their temperature relative to the density-peak temperature. If an ice layer is located above a freshwater reservoir that is warmed from below (RB configuration), several coupling regimes are possible, depending on the intensity of thermal driving. The entire water region is stably stratified and motionless for water temperatures lower than 4 °C (upper-left panel in Fig. 2g). In this condition, heat transfer

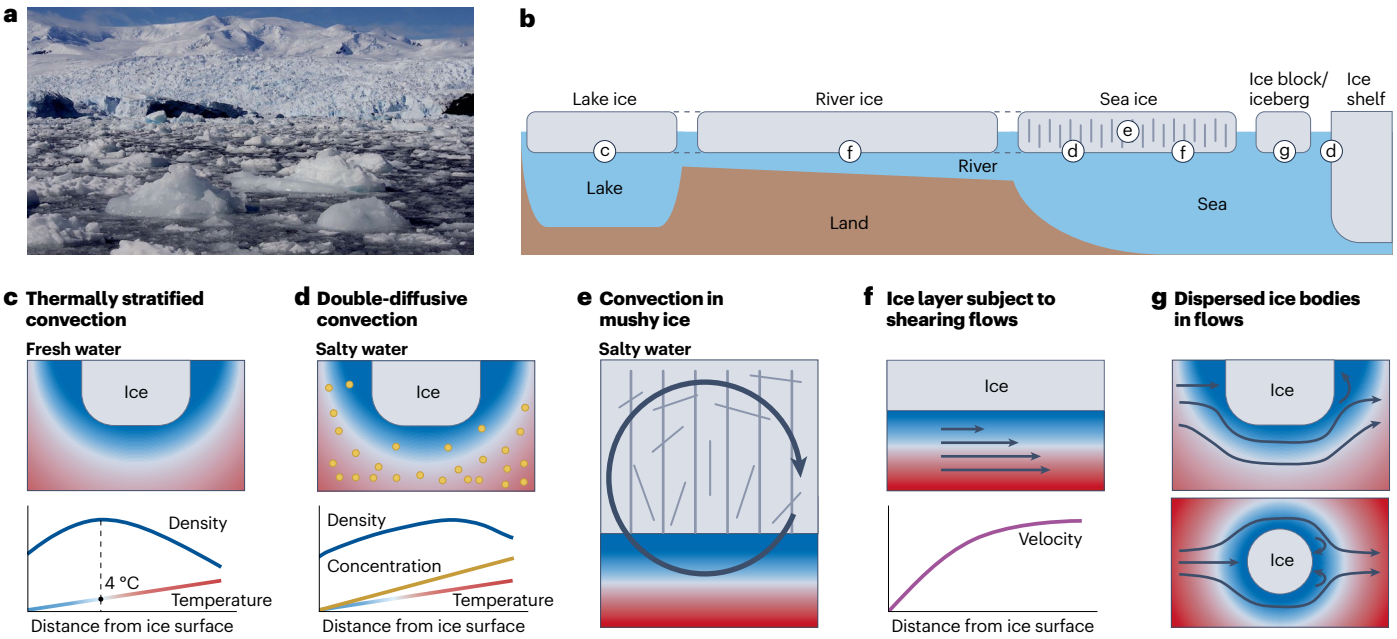

Fig. 1 | Interactions between ice and some typical flow conditions in the nearby water environment. Flow determines the local and global heat transfer process, thereby affecting the phase transition kinetics and the morphology of the ice–water interface. This in turn can influence the flow characteristics. **a**, A small tidewater glacier in the Antarctic. **b**, Typical flow configurations include stratified convection in fresh water, double-diffusive convection in salty water, brine convection in mushy ice, external flows moving along an ice layer, and external flows surrounding dispersed ice bodies. **c**, The temperature-induced density anomaly of water (lower panel) causes water between the freezing point and the density-peak temperature to be subject to a reversed buoyancy force. **d**, Because salts (yellow dots) are almost insoluble in ice, freezing and melting in salty water leads to salinity variations in the surrounding water. When ice melts in salty water, double-diffusive convection and vertical double-diffusive convection can occur because of the competing contributions to density from temperature and concentration gradients, as well as the disparity between thermal and solutal diffusivities (high Schmidt number). **e**, When salty water freezes, the water solidifies into ice and the salt is excluded to form saltier brine. The ice layer forms a porous mushy layer with unfrozen brine trapped in cavities and channels. Convection inside mushy ice is possible if the ice is sufficiently porous and becomes permeable. **f**, The shearing effect caused by the mean flow competes with the buoyancy effect. Together they determine the phase-change dynamics of the ice. **g**, For ice of finite size or transported by the flow, such as icebergs, different ice fronts encounter distinct flow fields, leading to a complex range of phenomena. Part **a** adapted with permission from ref. 22, James Gardner.

through the water layer is weak, resulting in a thick ice layer in the asymptotic thermal equilibrium state (light red regime in Fig. 2h). At higher thermal driving (increased bottom temperature), an unstably stratified water layer appears beneath the stably stratified water layer that is in contact with the ice. Initially, the buoyancy in the unstably stratified water layer is insufficient to trigger the onset of convection (upper-right panel in Fig. 2g). The heat transfer in the water remains diffusive and the ice layer remains thick (dark grey regime in Fig. 2h). When the thermal driving is further enhanced such that the onset of convection is reached in the bottom water layer, the resulting ice layer thins abruptly (lower-left panel in Fig. 2g and light grey regime in Fig. 2h). Finally, with even greater basal thermal driving the strong buoyancy in the unstably stratified water layer generates hot plumes that can penetrate the stably stratified layer and curve the ice front (lower-right panel in Fig. 2g and blue regime in Fig. 2h). The stably stratified water layer becomes extremely thin and exerts negligible influence on the equilibrium ice thickness. The effect of the water density anomaly vanishes[49] (Fig. 2g).

The multiple stratifications possible in water also allow for the existence of multi-equilibrium states depending on the initial conditions of the system[50]. The influence of stratification on phase-change dynamics and ice front morphology also occurs in FRB configuration cases (ice at bottom, thermal warming at the top)[47,51], in subglacial lakes under low ice overburden pressure[52], in turbulent shear flows[53] and in pipe flows[54]. Notably, there is an exchange in the gravitational stability of the water layers adhering to and away from the ice in FRB cases[47].

Freezing and melting in salty water

Effects of double-diffusive convection

Dissolving salt in water changes its freezing and melting dynamics relative to fresh water. Sea water is a hypoeutectic aqueous solution, whereas salts are almost insoluble in ice. Therefore, the freezing of salty water expels the salt from the ice matrix, and the melting of ice releases fresh water. As a result, freezing and melting in salty water are accompanied by substantial salinity variations in the liquid close to the ice front (Fig. 1d). The coupled effect of temperature and concentration defines a peculiar equation of state for salty water. In particular, for mass salt concentrations above about 2.7% for NaCl solution (about 2.5% for sea water), the thermal anomaly disappears and the phenomenon of reversed buoyancy is not present. At thermal equilibrium without ongoing phase change, different stratification modes can be found in the salty water beneath an ice layer subject to a hot boundary (Fig. 3a). For a high salt concentration, the salty water behaves like a positively buoyant liquid. The entire liquid region is gravitationally unstable, and

convection can occur under sufficient buoyancy driving because of a temperature difference between two boundaries (dark blue regime in Fig. 3a). For a low salt concentration, the density of salty water, like that of pure water, varies non-monotonically with increasing temperature. If the hot boundary is at a higher temperature than the density-peak temperature, the liquid region is composed of a stable stratification above an unstable one (light blue regime in Fig. 3a). Otherwise, the entire liquid region is gravitationally stable without convection[55] (dark grey regime in Fig. 3a).

More commonly, during the dynamical process of basal ice melting in salty water, both temperature and salt concentration increase with depth. The influence of salt concentration on density usually exceeds that of temperature, leading to a stable density background. Because the thermal diffusivity is much higher than the solutal diffusivity, a fluid parcel that is perturbed away from its neutral vertical position quickly adapts its temperature with negligible changes in its salt concentration. The difference between its density and that of its surroundings will thereby force it back to and even beyond its neutral position. This mechanism leads to an oscillatory process that characterizes the development of double-diffusive convection in the diffusive regime. The water layer is eventually destabilized into convectively mixed double-diffusive layers separated by sharp diffusive interfaces[56–60]. Similar double-diffusive layers are also observed in the solidification of hypereutectic aqueous solutions from below[61,62]. In such cases, the fresh and cold liquid rises with plumes and accumulates near the top to provide the downward temperature and concentration gradients[63].

High-resolution large-eddy simulation shows that double-diffusive convection controls the oceanic mixing and basal melting of ice

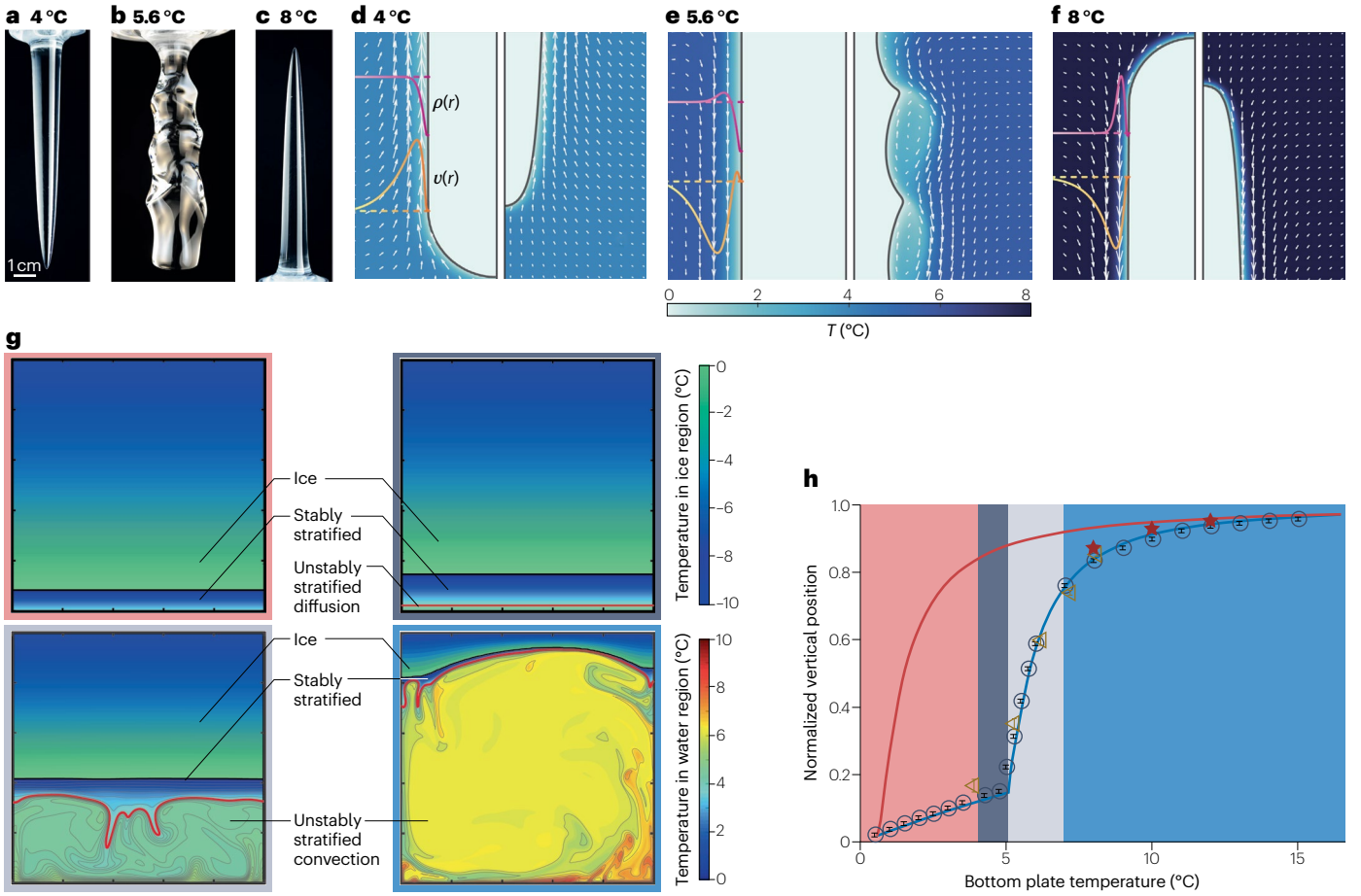

Fig. 2 | Freezing and melting coupled to stratified convection in fresh water. **a**–**c**, Typical morphologies of melting ice blocks submerged in fresh water with different ambient temperatures: 4 °C (part **a**), 5.6 °C (part **b**) and 8 °C (part **c**). **d**–**f**, Temperature field (colour) and velocity field (arrows) from simulations corresponding to the cases in parts **a**–**c** at early stages (left side of each part) and late stages (right side of each part). Curves sketch density (pink) and flow velocity (yellow) profiles at early stages. **g**,**h**, Freezing dynamics of water layer in Rayleigh–Bénard configuration at various bottom-plate temperatures. Part **g** shows temperature fields when the freezing of water from above reaches thermal equilibrium at different bottom temperatures: 3.8 °C (upper-left panel), 4.75 °C (upper-right panel), 5.5 °C (lower-left panel) and 10 °C (lower-right panel). Black lines indicate the ice–water interface and red lines indicate the instantaneous 4 °C isotherm. Coloured outlines correspond to the regions in part **h**. Part **h** shows average vertical positions of the ice front at equilibrium from experiments (brown triangles), 2D simulations (grey circles) and 3D simulations (red stars). A lower front corresponds to thicker ice. Blue line shows model predictions that account for thermal stratification within the water region due to the density anomaly. Red line shows model predictions without consideration of thermal stratification by neglecting the density anomaly. Shading indicates different flow dynamics regimes: weak heat transfer and thick ice (light red); stratification but not convection, with thick ice (dark grey); onset of convection and thinning of ice (light grey); strong buoyancy (blue). Parts **a**–**f** adapted with permission from ref. 46, APS. Parts **g**,**h** adapted with permission from ref. 49, PNAS.

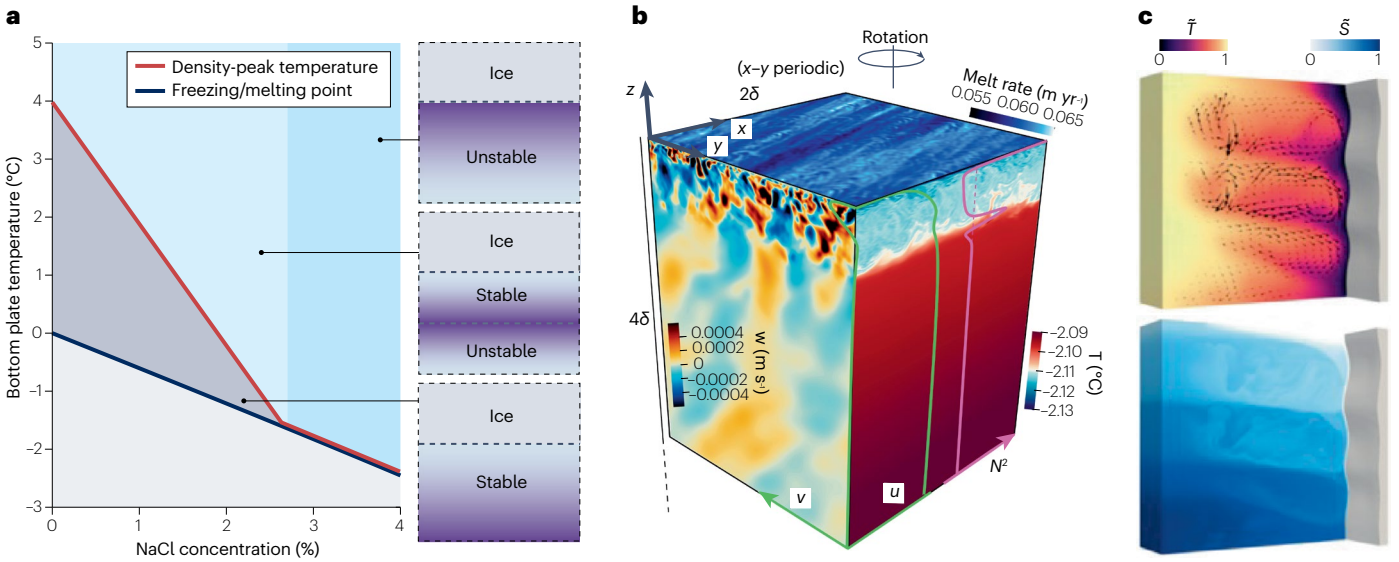

Fig. 3 | Stratification of salty water beneath ice and double-diffusion in ice melting process in salty water. a, The density-peak temperature (red line) and phase-change temperature (dark blue line) of aqueous NaCl (prime solute of sea water) solution as a function of NaCl concentration. For salty water beneath an equilibrium ice layer and subject to a hot boundary (right-hand sketches), different stratification modes are possible, corresponding to the coloured regimes in the temperature–concentration plot. **b**, Large-eddy simulation results of the basal melting of a horizontal ice layer above an ocean, with a slow external flow in the x-direction. The x–y plane displays the instantaneous melt rate, the y–z plane displays the vertical velocity w field, and the x–z plane displays the temperature T field. Green lines show the horizontal velocities in the x and y directions (u and v). Pink dashed and solid lines show the buoyancy frequency squared (N^2) at 0 h and 30 h. The rotational boundary-layer scale is $\delta \approx 5$ m. **c**, Direct numerical simulation on the side melting of an ice block in salty water. The Prandtl number is Pr = 10 and the Schmidt number is Sc = 1,000. Colour indicates the temperature field $\widetilde{T}$ (upper panel) and the salinity field $\widetilde{S}$ (lower panel). Part **b** reprinted with permission from ref. 64, PNAS. Part **c** is adapted from ref. 68, CC BY 4.0.

in a relatively warm and quiescent environment (Fig. 3b). The staircase-like structure controlled by temperature and salinity traps fresh and cold melt near the ice front as a stable diffusive sublayer. This diffusive sublayer grows over time, owing to the diffusion of salt, leading to a reduction in vertical transport and melting[64]. In the configuration of side melting of ice in salty water, the fresh melt ascends along the vertical ice front. It forms an upper stable zone where double-diffusive layers emerge from destabilization[65] (Fig. 3c). The double-diffusive layers can shape the morphology of an ice front. Valleys on the ice front correspond to the centres of these layers, and ridges correspond to the interfaces between them[66–69]. When ice melts from above, the buoyancy of the melt can drive strong turbulent convection which shapes a 'sharkskin' ice interface[70–72]. The buoyant convective motion of melt is also found to greatly enhance the melting[71,73,74]. That said, fresh and cold melt is not always lighter than its surroundings. Simulations on the lateral melting of an ice layer show that the competition between temperature-induced buoyancy and concentration-induced buoyancy can lead to the weakest flow being near the ice front and consequently a minimum melting rate[68].

Effects of convection in mushy ice

As mentioned above, during the growth of sea ice, water freezes into pure ice while the salt is expelled into the unfrozen saltier brine pockets. Sea ice, with brine trapped inside, is therefore a porous mushy layer (lower panel of Fig. 4a), in contrast to the dense and transparent ice layer formed in pure water (upper panel of Fig. 4a). Sufficiently porous mushy ice is permeable. With strong buoyancy driving, convective motion can occur inside the mushy layer[75,76] (Figs. 1e and 4b). The buoyancy-driven convection in the mushy ice causes the brine, which is saltier and of a lower freezing point than the bulk liquid, to flow out of the ice. This process promotes the formation of brine channels (chimneys) extending from the interior to the interface in the ice matrix, owing to a positive feedback mechanism involving increased local melting and reduced flow resistance in the outflow region. In the presence of chimneys, the liquid in a mushy layer initially flows uniformly toward the cold boundary. The liquid then moves horizontally towards the inlets of chimneys along the boundary and eventually drains into the liquid region through the chimneys. This phenomenon has been observed in the freezing of hypoeutectic solutions from above[77] and in the solidification of hypereutectic solutions from below[78]. Schlieren and direct imaging of salty water freezing from above in a Hele–Shaw cell show that convective drainage through active long streamers accounts for a large part of the ice desalination process[79,80].

The fluid mechanics of convection in mushy layers and brine drainage have been discussed elsewhere[61,62,81–83]. Various attempts have been made to mathematically model the growth of mushy ice[84–87]. In this section, we focus on how the convection affects the freezing process. Convection inside the mushy ice replaces the residual brine with fresher liquid that freezes at a higher temperature. This introduction of liquid that freezes more readily promotes further freezing and consequently lower porosity of the ice[76,77]. At the interface, numerical simulations show that the plumes through the chimneys into the liquid greatly alter the flow field and transform the local ice front from an undulate shape to a peak at the chimney outlet[88]. Meanwhile, the residual liquid carried by the plumes to the opposite boundary can possibly establish a concentration gradient there and induce double-diffusive layers[77].

Remarkably, combined experiments and theoretical modelling indicate that convection in the mushy ice enhances the heat transfer across the ice. The heat released from freezing can be transported more efficiently away from the ice–liquid interface towards the cold boundary so the ice growth gets promoted. A thicker ice layer in turn increases the intensity of buoyancy driving and aids convection. The equilibrium ice thickness is determined by the mode of coupling between liquid motions inside the porous ice and in the stratified liquid layer. The former depends on the strength of buoyancy driving in the mushy phase. The latter, as mentioned in the previous subsection, depends on the salt concentration and the effective buoyancy driving in the unstable stratification[55].

Freezing and melting with external flows

Ice layer subject to shearing flows

In the environmental context, an ice layer is often influenced by the movement of fluids beneath it: river flows, tides and large-scale ocean currents, among others (Fig. 1f). The dynamics of the water beneath the ice layer are governed both by buoyancy resulting from temperature variations and by shear stress from the externally imposed flow. The effect of shearing flows on the interface dynamics of an ice layer is typically investigated with numerical simulations in the following configuration: a horizontally extended solid layer grows or melts above an externally imposed flow of its melt parallel to the solid–liquid interface (Fig. 5a). To elucidate the coupled effect of shear and buoyancy, these studies commonly use liquids with positive buoyancy, resulting in an unstably stratified liquid region beneath the solid layer. They often consider a mean flow driven by either constant pressure gradient (Fig. 5a) or prescribed wall shear, known as Poiseuille–RB or Couette–RB with a melting or freezing boundary.

These studies reveal how the morphology of the solid–liquid interface varies depending on the relative magnitudes of buoyancy and shear in the liquid beneath[53,89]. As discussed above, in the absence of shear and when only natural convection is created by heating from below, the large-scale convecting cells create dome-like patterns on the underside of the solid layer (Fig. 5b,c). The organization of these dome-like patterns depends on the strength of the thermal driving, which is parameterized by the Rayleigh number (Ra) in the liquid layer. The patterns have a hexagonal-like horizontal tessellation at low Ra (ref. 41) and become larger and more irregular as Ra increases. If shearing flow is present, the interface tends to be homogenized along the mean flow direction (Fig. 5d). At higher shear intensities, the formation of large-scale meandering rolls results in a quasi-2D pattern on the interface, characterized by ridges and grooves aligned with the mean flow direction (Fig. 5e). Finally, as shear intensity further increases, the patterns on the interface tend to disappear (Fig. 5f).

Another intriguing phenomenon observed on the solid–liquid interface under shearing flows is the presence of travelling interfacial waves (Fig. 5g,h). As already mentioned, large-scale circulations of the buoyancy-driven convection sculpt dome-like patterns on the solid–liquid interface in the absence of a mean flow. If the mean flow is enough to horizontally transport the convection rolls but not so strong as to break their structural coherence, the dome-like patterns can migrate in the downstream direction (Fig. 5g). This migration forms travelling interfacial waves and causes the local solid layer thickness to vary periodically over time and space[90,91] (Fig. 5h). Travelling interfacial

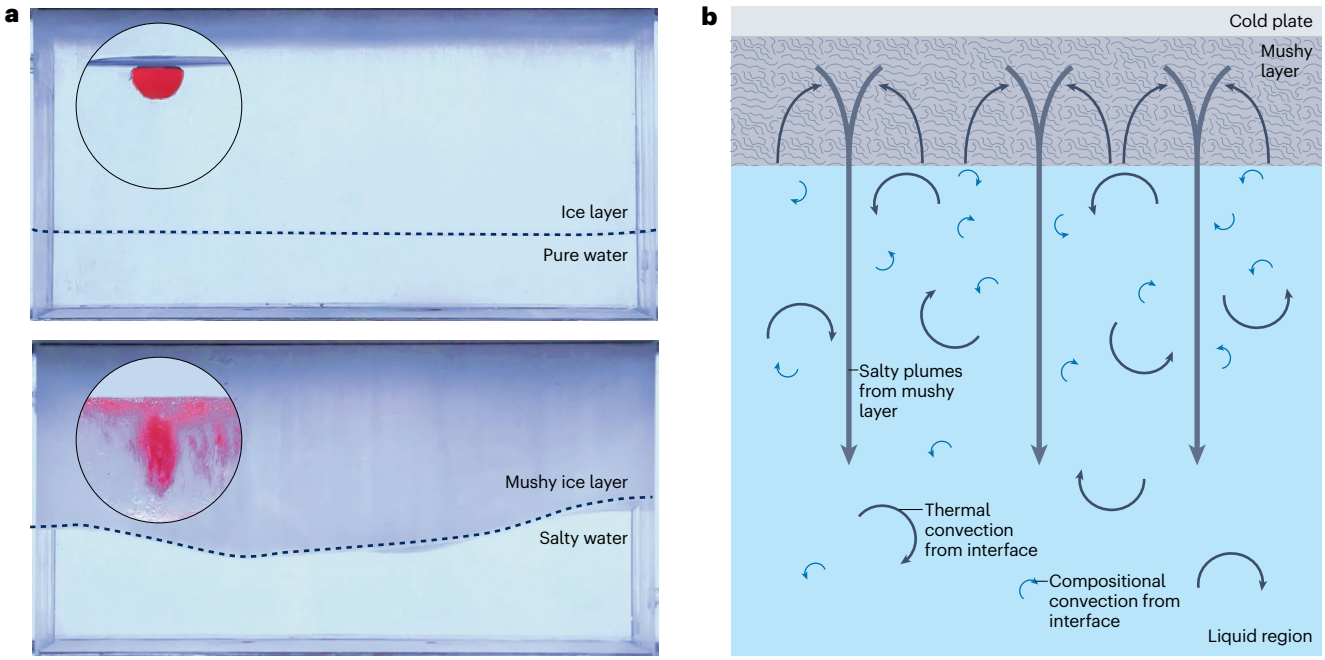

Fig. 4 | Ice formation in pure water and salty water, and the convection motion inside porous ice. a, Comparison between the ice layer frozen in pure water (upper panel) and in salty water (lower panel). The insets show the results of adding dye to the ice layer: freshwater ice is dense and saltwater ice is porous. **b**, Schematic diagram indicating the convection types that occur during the freezing of salty water from above. Aside from convections driven by temperature and salinity gradients from the interface, convection can emerge from the interior of the mushy ice and release the residual saline into the liquid region with plumes, accompanied by a return flow of fresher water. Part **a** adapted with permission from ref. 55, CUP. Part **b** reprinted with permission from ref. 77, CUP.

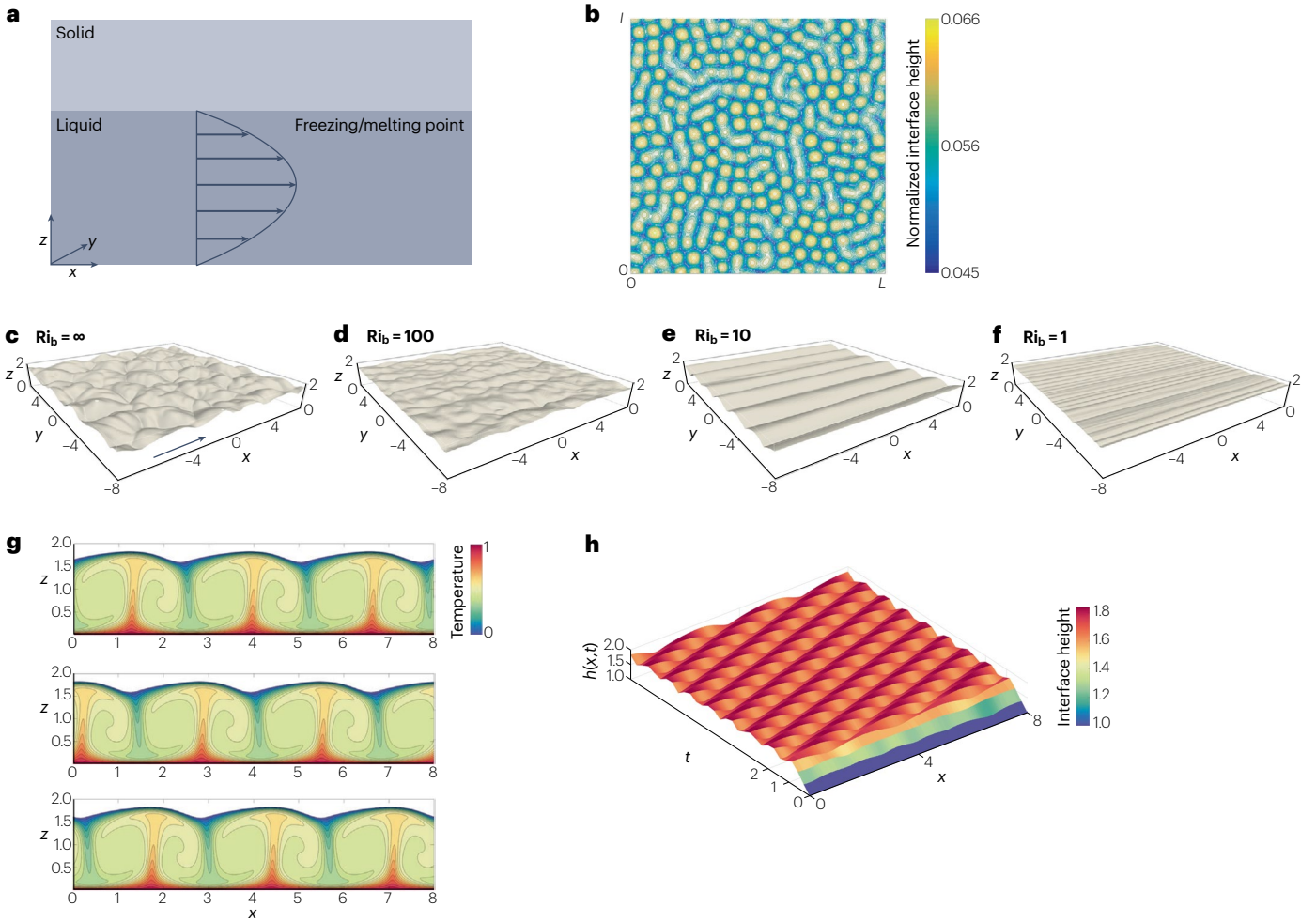

Fig. 5 | Combined effects of buoyancy and shear on solid–liquid interface morphology. a, Sketch of a solid layer melting above an unstably stratified shearing flow driven by a constant pressure gradient. **b**, Interface morphology of a solid layer subject to turbulent thermal convection of its melt, from a 3D simulation. The effective Rayleigh number in the liquid region is $Ra = 1.76 \times 10^4$ and the Prandtl number is $Pr = 10$. The height of the interface is non-dimensionalized by the total height of the system. The length and width of the system are both L. **c**–**f**, Interface morphologies during the melting of a solid layer above an unstably stratified mean flow of its melt at different mean flow intensities, indicated by the bulk Richardson number Ri_b. In these simulations, $Ra = 1.25 \times 10^5$ and $Pr = 1$. The mean flow is driven by a constant pressure gradient. The arrow in part **c** indicates the direction of the mean flow. **g**,**h**, Travelling interfacial waves at the base of a melting solid layer above an unstably stratified shearing mean flow of its melt. The initial dimensionless thicknesses of the solid layer and liquid layer are both 1. $Ra = 4.64 \times 10^4$ and $Pe = 20$. Part **g** shows interface morphologies and temperature fields (colour) in the liquid from simulations at different times. Part **h** shows the spatiotemporal evolution of the solid–liquid interface. Parts **a** and **c**–**f** adapted with permission from ref. 89, CUP. Part **b** adapted with permission from ref. 41, APS. Parts **g**,**h** adapted with permission from ref. 91, CUP.

waves are experimentally observed on the ice front subject to a turbulent flow (such as in pipe flows[92]) and predicted to most likely exist during melting or slow growing of ice[93]. Waves of large amplitude can further evolve into ripple or scallop patterns when flow separations occur near the crests[93]. Visualization of water flow over the upper surface of an ice layer highlights that these patterns arise from the positive feedback between the ice front morphology and the high level of turbulent kinetic energy production in the recirculating eddy downstream of the crest[94]. A similar mechanism accounts for the formation of the ripple or scallop patterns on the surface of a dissolving solid[95,96].

The coupled effect of shear and buoyancy is also relevant for the heat transfer across the liquid layer and the phase-change dynamics. As the amplitude of horizontal shear increases from zero, vertical heat transfer across the liquid is initially suppressed and then reinforced[97,98]. This dependence of heat transfer on shear explains in turn how several other quantities depend non-monotonically on the shear intensity: the freezing and melting rates[89], equilibrium solid layer thickness[91] and solid–liquid interface roughness[89,90].

Flow structures in contact with ice and ice morphology resulting from melting are not only affected by externally imposed pressure gradients and wall shear but also depend on system rotation. For example, rotation tends to produce thinner and many more dome-like patterns on the solid–liquid interface during the basal melting of a solid layer compared with the case without rotation[99]. In the presence of a strong

mean flow, the introduction of system rotation affects the orientation of the ridges and grooves on the interface. For large shearing intensities, the introduction of system rotation can induce wavelike evolution of the interface[89]. These effects of rotation are relevant for understanding ice phenomena on Earth[100] and other rotating celestial bodies[101].

Dispersed ice in flows

So far, we have reviewed the freezing or melting in fresh water or salty water where an ice body is extended and fixed in space, serving as a system boundary. It is interesting to ask how the phenomenology changes when the ice has a limited spatial size or is transported by the flow (Fig. 1g). This has been considered in laboratory studies on the melting of dispersed ice bodies subject to a flow far from any boundary[102,103]. For an ice block floating but held stationary in space in a uniform incoming flow of salty water (Fig. 6a) — modelling an iceberg — experiments, aided by numerical simulations, show that melting is faster on the vertical sides than on the bottom. At large relative ambient flow speeds, the external flow can detach the cold melt from the ice surface, allowing the warm inflow water to contact the ice surface (Fig. 6b). Local melting on the bottom occurs faster in the region where the melt is detached than in the region with attached melt (Fig. 6b). The accelerated melting due to melt detachment also applies to the vertical surfaces. The greatest enhancement occurs on the upstream ice front directly facing the inflow. Consequently, the geometrically averaged melting rate per unit interface area increases with increasing ambient flow velocity but decreases with increasing length–height aspect ratio[102,104] (Fig. 6c).

An orientation-dependent melting rate is also observed for the melting of spherical ice bodies submerged in uniform inflows of water[105,106] (Fig. 6d). For a spheroidal ice body of a fixed volume, if the length–width aspect ratio is larger, then the surface area directly facing the inflow, with the most intense melting, is smaller, but the overall surface area is larger. The reduction in surface area facing the inflow tends to decrease the overall melting, whereas the increase in total surface area tends to increase it. This competition leads to a non-monotonic trend in the melting rate for different shapes. The minimum melting rate is attained when the long body side is in the streamwise direction[103]. Interestingly, despite the complex morphology of the downstream ice front due to flow separation, in these experiments and simulations the upstream ice front always converges to a typical shape during the fusion of ice spheres[103,106] (Fig. 6d). This self-similar evolution of ice front is the result of the coupling between its shape and the boundary-layer flow along it, as predicted by theoretical analysis[107]. Such a two-way coupling also explains the angular or rounded interface shape due to erosion or dissolution of a fixed solid body in fast unidirectional flows[108–110] (Fig. 6e,f). Similarly, the upper interface of a melting or dissolving solid is sculpted through its interaction with the buoyancy-driven boundary-layer flow. Theoretical analyses show that the interface universally takes the shape of a parabola sufficiently near its tip, whereas

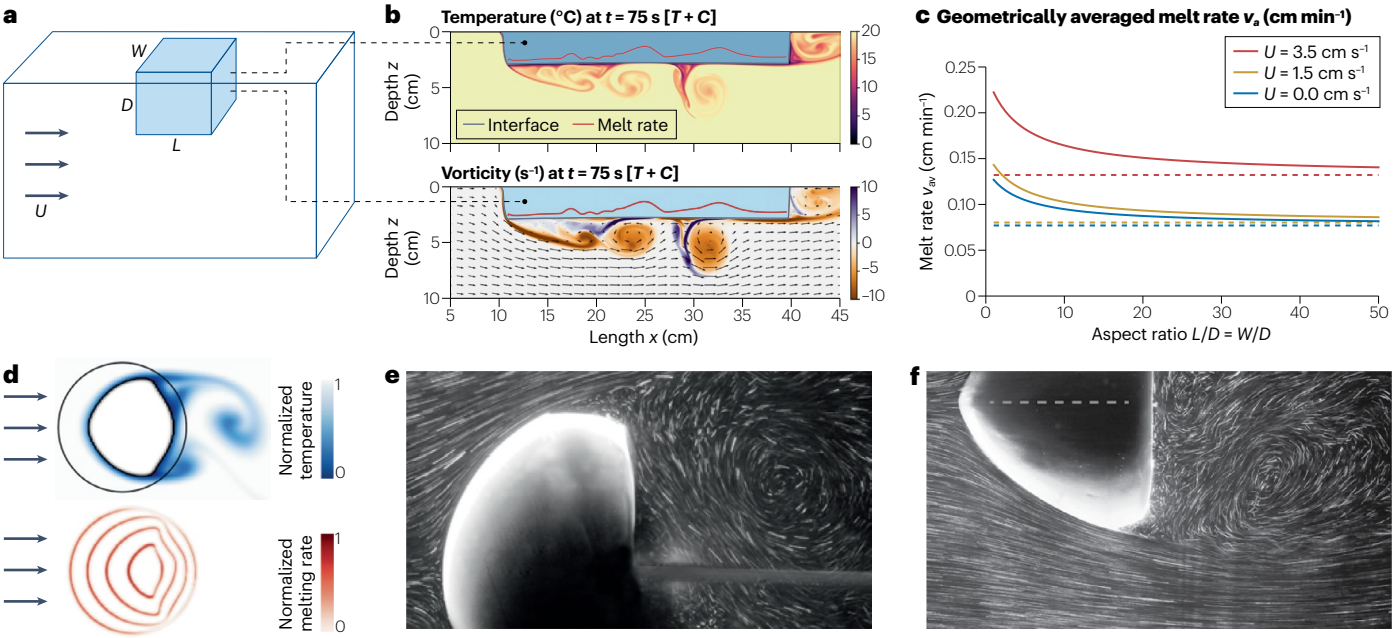

Fig. 6 | Melting of dispersed ice bodies subject to external flows. a–c, Melting of an iceberg floating on the uniform inflow of salty water. The scenario can be modelled as salty water flowing past a floating iceberg of length L, width W and immersed depth D (part **a**). The incoming salty water is of ambient salt concentration 30 g kg^{-1}, ambient temperature 20 °C and uniform ambient velocity U. Simulations with temperature, salinity, and buoyancy effects turned on (T + C) yield an instantaneous temperature field (upper panel of part **b**), vorticity field (colour map in the lower panel of part **b**) and velocity field (arrows in the lower panel of part **b**). Red lines show qualitatively the melting rate at different locations on the ice block bottom. Geometrically averaged melting rates shown with solid lines (per unit ice–water interface area) are obtained from experiments as a function of the length–height aspect ratio and the width–height aspect ratio for different ambient flow velocities (part **c**). The dashed lines are used to illustrate the corresponding basal melt rates for each velocity. **d**, Simulations of melting of a spherical ice body subject to a uniform inflow. **e**,**f**, Experimental interface morphologies and visualized flow fields during the dissolving (part **e**) and eroding (part **f**) of a spherical body subject to uniform inflows. Parts **a** and **b** adapted with permission from ref. 102, APS. Part **c** reprinted with permission from ref. 102, APS. Part **d** is adapted from ref. 103, CC BY 4.0. Part **e** adapted with permission from ref. 109, CUP. Part **f** adapted with permission from ref. 110, PNAS.

its broader profile forms a rich variety of shapes. These findings are verified by experiments and numerical simulations[111–113].

For ice spheres freely advected by a turbulent flow (as inertial particles), the possibility of rotating allows the spheres to maintain their spherical shape for a long time. This extra degree of freedom may also lead to stronger surface heat flux and melting as the dynamic and thermal boundary layers can fully develop[114]. The problem of melting objects under the Lagrangian representation at the laboratory scale has been studied[114] but remains largely unexplored so far. We think that many other phenomena might be of interest, for instance the role of salinity on the melting of transported ice blocks and the collective effects arising from multibody interactions[115].

Applications at the cryosphere and hydrosphere interface

In the natural environment, freezing and melting in the presence of flows occur at the interface between the cryosphere and hydrosphere[116]. These phenomena encompass a variety of processes involving sea ice, lake and river ice, snow covers and glaciers.

Melt ponds, under-ice melt ponds and false bottoms

Melt ponds are a distinctive feature of the summer polar sea-ice cover[117] (Fig. 7a). They form owing to solar-radiation-induced melting of snow and ice. The accumulation of melt water into pre-existing uneven topography leads to the formation of typically shallow (≤1 m) freshwater reservoirs[118]. Melt ponds are important for the climate owing to their role in a positive feedback mechanism involving albedo[119]. As opposed to ice, the water masses of ponds are good absorbers of solar radiation. The presence of ponds reduces the terrestrial albedo, which in turn increases surface temperature and promotes further pond expansion. This phenomenon is responsible in the Arctic for a strong correlation between the area fraction covered by melt ponds in spring and the extent of sea ice in September[120]. Several models have been proposed for the evolution of single melt ponds[121] and for the collective dynamics of melt pond networks[122,123]. Small-scale understandings of Arctic melt ponds are difficult, and a numerical modelling approach can provide useful information. Direct numerical simulation demonstrates the existence of an abrupt transition from a fully frozen equilibrium state to one featuring a distinct melt pond as the radiation intensity and initial depth of the melt pond increase[124]. This bifurcation is associated with the onset of turbulent convection in the melt pond, which complies with the dynamics and scaling relations of stratified convection in the FRB configuration. The water in melt ponds, slightly warmer on the top relative to 0 °C at the bottom, undergoes reversed-buoyant turbulent convection once the buoyancy is strong enough. Heat is effectively transported to the ice–water interface to maintain the depth of the melt pond (Fig. 7b). In addition, the importance of the geometry of

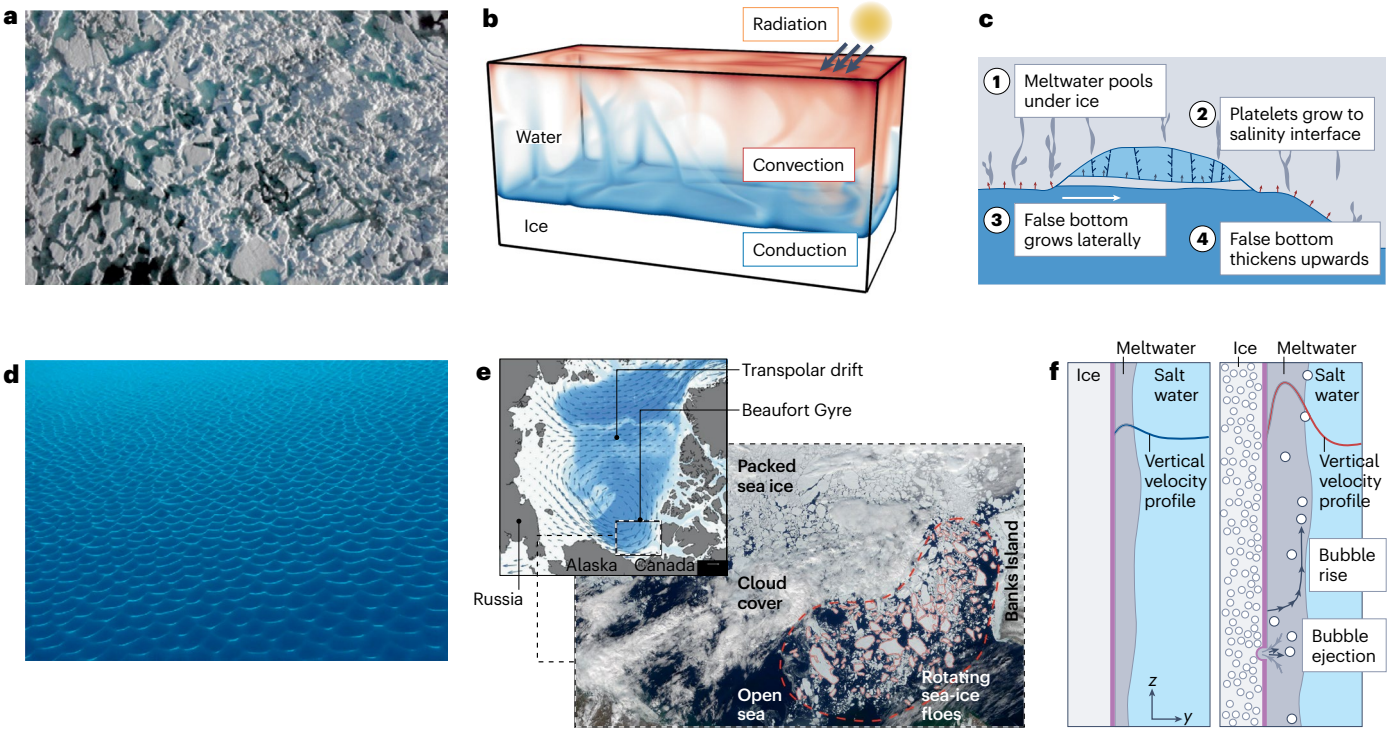

Fig. 7 | Some example scenarios of freezing and melting in the presence of flows in the cryosphere. a, Melt ponds on summer Arctic sea-ice cover. **b**, Snapshot from a direct numerical simulation in a simplified physical modelling system, showing the temperature field in a stable melt pond. **c**, Formation and thickening mechanisms of the false bottom (secondary ice layer) at the interface between under-ice melt pond and ocean. The small arrows indicate the movement of the ice–water interface. **d**, Scallops on the submerged side of a free-drifting iceberg. **e**, Spinning ice floes in the marginal ice zones in the western Arctic Ocean. Inset: the Arctic Basin, with the area corresponding to the main image highlighted. **f**, Comparison of meltwater plumes in the melting of clear ice (without bubble, left) and glacier ice (with pressurized bubble, right). Blue and red lines show the vertical velocity profiles for the meltwater plumes. Part **a** adapted with permission from ref. 165. Part **b** adapted with permission from ref. 124. Part **c** adapted with permission from ref. 128. Part **d** adapted with permission from ref. 166. Part **e** adapted with permission from ref. 143. Part **f** adapted with permission from ref. 144.

Glossary

Advection
The transport of a substance or quantity by fluid motion.

Albedo
The ratio of solar radiation reflected from the Earth's surface to the solar radiation received by the Earth's surface.

Convection
The relative motion of different parts of a fluid. When temperature or concentration gradient exists in the fluid, convection caused by buoyancy due to density inhomogeneity is called natural convection. Forced convection is driven by external forces, such as a pump or a fan.

Couette
Couette flow is the flow of a viscous fluid between two parallel surfaces moving relative to each other.

Cryosphere
The part of the Earth's surface where water exists in solid form. In this Perspective, we refer in particular to sea ice, river and lake ice, snow covers and glaciers.

Diffusion
The transport of mass or energy from a region of high concentration to a region of low concentration due to the thermal motion of atoms, ions and molecules.

Diffusivity
The rate at which mass or energy can diffuse in a substance.

Double-diffusive convection
Double-diffusive convection occurs when the fluid density in a system is affected by two components; often the diffusivities of the two components are different.

Equation of state
The equation of state characterizes the relationship between the density of a fluid and its pressure and temperature.

First-year sea ice
First-year ice is typically thicker than 30 cm but has not survived a summer melt season.

Hele–Shaw cell
Hele–Shaw flow refers to the slow flow of a fluid between two parallel flat plates separated by a narrow gap. In certain specific configurations, Hele–Shaw cells can be used for the visualization of the flow field in 2D.

Hydrosphere
The sum of water on, under, and above the Earth's surface in forms of gas, liquid and solid. In this Perspective, we refer in particular to water in liquid form.

Hypereutectic
In a liquid eutectic system, solute and solvent solidify simultaneously into a mixture as the temperature drops. A hypereutectic composition, having more solute and less solvent than the eutectic, causes solute to solidify first.

Hypoeutectic
A hypoeutectic composition has less solute and more solvent, resulting in the solvent solidifying first as the temperature drops.

Lagrangian representation
Lagrangian representations focus on the properties of fluid parcels or objects that move in space with time. Conversely, Eulerian representation focuses on the properties at specific locations in space.

Latent heat
The energy released or absorbed by a substance as it changes from one phase to another in a constant-temperature process, for example by freezing or melting.

Multi-year sea ice
Ice that has survived a summer melt season and is much thicker than younger ice, typically 2–4 m thick.

Permeability
The ability of a porous material to allow fluids to pass through it.

Poiseuille
Poiseuille flow refers to the flow of a viscous fluid in a channel or pipe driven by pressure difference.

Porosity
The ratio of void volume to total volume of a material.

Rayleigh–Bénard convection
An idealized model of natural convection. The fluid is confined between a hotter bottom boundary and a parallel colder top boundary. The temperature difference leads to density difference, inducing buoyancy that drives the convection.

Supercooled water
Liquid water with a temperature below the freezing point.

Vertical convection
Vertical convection models natural convection confined between two parallel vertical boundaries with different temperatures.

the melt pond in the evolution of a single melt pond has been examined with large-eddy simulations[125]. The impact of heat-flux scaling laws on the total surface ablation rate and the probability distributions of pond surface areas has been assessed with finite difference simulations[126].

Besides collecting into melt ponds, surface melt water can drain under the ice through pores, cracks and edges[127] and accumulate into under-ice melt ponds (under-ice meltwater layers). Such an under-ice melt pond and the ocean beneath, separated by a diffusive interface, form a similar structure to the double-diffusive layer discussed above. Further, a secondary ice layer (also known as a false bottom) can grow at the diffusive interface[128] (Fig. 7c). Its formation is the combined result of both double-diffusion at the interface and the reversed-buoyant convection in the under-ice melt pond. When the sea water below the under-ice meltwater layer is colder than 0 °C, the more rapid diffusion of heat relative to salt cools the fresh water near the interface while maintaining the salt concentration at a low level. Supercooled water rises owing to the density anomaly, and freezes at the bottom of the old ice layer. Vertical platelet ice then grows downward to the interfacial region, where it triggers the refreezing of supercooled meltwater and serves as anchor points in the lateral growth of the false bottom[129] (Fig. 7c). Under-ice melt ponds and false bottoms isolate the old ice layer from the ocean. This isolation reduces the transport of heat, mass and momentum and leads to a thicker ice layer, longer sea-ice lifespan and larger sea-ice coverage area[130,131]. However, the latent heat released during the formation of a false bottom brings new effects. It results in upward heat flux into the old ice layer[130] and downward heat flux into the mixed layer in the ocean, having regional consequences for the overall ice pack[131]. Laboratory results on the influences of double-diffusive layers can be extended to under-ice melt ponds and false bottoms, subject to the caveats discussed below. Laboratory studies at controlled conditions allow for isolating individual forces and effects. Despite smaller scales and differing control parameters from large-scale geophysical phenomena, laboratory experiments and simulations are essential for understanding small-scale processes needing parameterization in global and regional models.

Ice covers, ice shelves and icebergs

The ice–water coupling processes discussed above are also encountered on the surfaces of ice covers, ice shelves and icebergs. For example, the basal melting and refreezing of the Ross Ice Shelf is controlled by ocean mixing and transport via tidally modulated double-diffusive convection[132]. In a permeable ice layer, full-depth desalination due to gravitational brine convection can occur. It promotes the transition from first-year sea ice to multi-year sea ice and leads to anomalies of seawater salinity[133–136]. As demonstrated in laboratory studies, different levels of couplings of buoyancy and shear produce different interface morphologies. This result can help to understand how fine-scale flow conditions in the ocean determine the scallops, ripples and other patterns observed at different locations in a basal crevasse (crack) at the Ross Ice Shelf[137]. The ablation of swiftly shearing flow also explains the scallop patterns observed on the sides of melting icebergs (Fig. 7d), within water-filled ice caves and on the lower surface of ice cover in rivers[138,139]. The mixing and heat transfer relevant for these systems are intensified by rapid turbulent flow. Hence, faster flow of water limits the thickness of local river ice cover compared with where the flow is slower. As a result, ice thickness on meandering rivers varies laterally[140]. The study of ice body transportation in flows is also tightly related to the description of iceberg life cycles[141], understanding the trajectories of isolated ice floes[142], and investigating under-ice eddy fields and their connections to large-scale ocean currents[143] (Fig. 7e).

There are even more complicated interactions between ice and the surrounding water flow, interactions that involve gases and air (multiphase and multicomponent phenomena). These interactions are not reviewed in detail in this Perspective, but we note here that understanding them also benefits from laboratory studies. One example is the acceleration of natural glacier melting due to the release of compressed air bubbles. As snow compacts to form glacial ice, air is trapped within the ice as bubbles. The bubbles are compressed as the ice descends within the glacier. The pressurized bubbles are ejected into the ocean as the extremity of glacial ice melts in the ocean. Laboratory experiments and theoretical analysis find that the ejection and rise of bubbles add to the turbulent kinetic energy in the boundary layer by providing additional impulse and buoyancy. As a result, the melting rate is much faster for natural glacier with bubbles (right panel of Fig. 7f) than for clear ice without bubbles[144] (left panel of Fig. 7f). In addition, the collective dynamics of sea-ice floes in open water involves processes such as collisions, rafting, ridging, fracturing and welding. These processes are currently parameterized in geophysical-scale sea-ice codes[115,145] but they still need fundamental, that is, small-scale, understanding. Some successful examples of investigations include experiments on pancake ice rafting due to wind and wave[146], the wave-induced breaking of freshwater ice covers[147] and the initial sea-ice growth influenced by wind[148].

Discussion

Clearly, terrain measurements remain the most suitable method for investigating ice-related geophysical processes. This is because the variety and complexity of these phenomena, involving wide scale ranges, multiple components and intricate feedbacks, cannot be easily schematized. Laboratory studies, conversely, allow for optimally controlled conditions. They often work in closed systems (such as the RB cell and other relevant systems) with well-prescribed boundary conditions or with flows whose spatial and temporal dependence is imposed by the experimenter. This makes it possible to isolate and evaluate the impact of individual forces and effects.

Evidently, any extrapolation to the environmental scale must be done with caution. First of all, because one is dealing with nonlinear phenomena, the principle of superposition of effects does not apply. Second, the scales in the laboratory are smaller. They correspond to dimensionless control parameters that often differ by many orders of magnitude from large-scale geophysical phenomena. However, laboratory experiments and fully resolved simulations seem to be suitable tools for understanding processes that take place at small scales (smaller than those of global and regional numerical models) that require parameterization. This is the case, for example, with the problem of melt ponds as discussed above.

For the purpose of weather or climate prediction, substantial effort has been devoted to incorporating ice into coarse-grained geophysical models[149–158]. Controlled and repeatable laboratory studies on the coupled physical mechanisms of freezing and melting in complex flow conditions can contribute to a further understanding of the physics underlying relevant geophysical processes. This understanding, in turn, would promote the parameterization of the ice–water interactions and aid the development of large-scale ice models[141,159–163], as well as aiding in comprehending, parameterizing, predicting and possibly using these natural processes[164].

Outlook

The field of fluid dynamics is characterized by a rich phenomenology, which is ultimately linked to its equations – that is, the Navier–Stokes equations, which are nonlinear and can have a large number of degrees of freedom. When fluid flows are coupled to other physical processes, such as heat and mass transport, they lead to an even greater variety of phenomena. Phase-change processes build on this rich landscape because, in the fluid dynamics context, they are unavoidably coupled to flows driven by temperature and salinity gradients. We have focused on reviewing melting and freezing processes in canonical flow configurations, but much remains to be explored.

Collaborative efforts are needed in experiments, numerical simulations and model development to better understand the following issues:

- Broad characterization of the role of ice body shape in melting and freezing processes in fresh and salty water flows. Understanding the formation of morphological patterns on ice interfaces with water and air.
- The role of inclusions and impurities, such as particles and bubbles in the ice matrix, and gases dissolved in the liquid, on the freezing and melting dynamics.
- Lagrangian transport properties of ice bodies in flows, encompassing laminar, wavy and turbulent flows, and the study of mechanical properties of ice (ice–water as a flow–structure interaction problem).
- Improved characterization of the dynamical role of radiative transfer in melting and freezing dynamics under different flow conditions.
- Freezing and melting processes under extreme thermodynamic conditions, such as high pressure and low temperatures. This is relevant not only for the understanding of subglacial terrestrial lakes but also for ice on extraterrestrial planets and icy moons.

Published online: 30 September 2024

References

1. Shepherd, A. et al. Greenland ice sheet motion coupled with daily melting in late summer. *Geophys. Res. Lett.* **36**, L01501 (2009).
2. Notz, D. The future of ice sheets and sea ice: between reversible retreat and unstoppable loss. *Proc. Natl Acad. Sci. USA* **106**, 20590–20595 (2009).
3. Tietsche, S., Notz, D., Jungclaus, J. H. & Marotzke, J. Recovery mechanisms of Arctic summer sea ice. *Geophys. Res. Lett.* **38**, L02707 (2011).
4. Hanna, E. et al. Ice-sheet mass balance and climate change. *Nature* **498**, 51–59 (2013).
5. Bintanja, R. & Van de Wal, R. S. W. North American ice-sheet dynamics and the onset of 100,000-year glacial cycles. *Nature* **454**, 869–872 (2008).
6. Alley, R. B., Clark, P. U., Huybrechts, P. & Joughin, I. Ice-sheet and sea-level changes. *Science* **310**, 456–460 (2005).
7. Jacob, T., Wahr, J., Pfeffer, W. T. & Swenson, S. Recent contributions of glaciers and ice caps to sea level rise. *Nature* **482**, 514–518 (2012).
8. Lambeck, K., Rouby, H., Purcell, A., Sun, Y. & Sambridge, M. Sea level and global ice volumes from the last glacial maximum to the Holocene. *Proc. Natl Acad. Sci. USA* **111**, 15296–15303 (2014).
9. Clark, P. U., Alley, R. B. & Pollard, D. Northern Hemisphere ice-sheet influences on global climate change. *Science* **286**, 1104–1111 (1999).
10. Golledge, N. R. et al. Global environmental consequences of twenty-first-century ice-sheet melt. *Nature* **566**, 65–72 (2019).
11. Curry, J. A., Schramm, J. L. & Ebert, E. E. Sea ice–albedo climate feedback mechanism. *J. Clim.* **8**, 240–247 (1995).
12. Perovich, D. K., Grenfell, T. C., Light, B. & Hobbs, P. V. Seasonal evolution of the albedo of multiyear Arctic sea ice. *J. Geophys. Res.* **107**, 8044 (2002).
13. Stroeve, J. & Notz, D. Changing state of Arctic sea ice across all seasons. *Environ. Res. Lett.* **13**, 103001 (2018).
14. Post, E. et al. Ecological consequences of sea-ice decline. *Science* **341**, 519–524 (2013).
15. Boetius, A., Anesio, A. M., Deming, J. W., Mikucki, J. A. & Rapp, J. Z. Microbial ecology of the cryosphere: sea ice and glacial habitats. *Nat. Rev. Microbiol.* **13**, 677–690 (2015).
16. Duprat, L. P. A. M., Bigg, G. R. & Wilton, D. J. Enhanced Southern Ocean marine productivity due to fertilization by giant icebergs. *Nat. Geosci.* **9**, 219–221 (2016).
17. Horvat, C. et al. The frequency and extent of sub-ice phytoplankton blooms in the Arctic Ocean. *Sci. Adv.* **3**, e1601191 (2017).
18. Wadham, J. L. et al. Ice sheets matter for the global carbon cycle. *Nat. Commun.* **10**, 3567 (2019).
19. Smith, A. W., Skilling, D. E., Castello, J. D. & Rogers, S. O. Ice as a reservoir for pathogenic human viruses: specifically, caliciviruses, influenza viruses, and enteroviruses. *Med. Hypotheses* **63**, 560–566 (2004).
20. Obbard, R. W. et al. Global warming releases microplastic legacy frozen in Arctic sea ice. *Earths Future* **2**, 315–320 (2014).
21. Peeken, I. et al. Arctic sea ice is an important temporal sink and means of transport for microplastic. *Nat. Commun.* **9**, 1505 (2018).
22. Gardner, J. How water, wind, waves and ice shape landscapes and landforms: historical contributions to geomorphic science. *Geomorphology* **366**, 106687 (2020).
23. Weeks, W. F. & Campbell, W. J. Icebergs as a fresh-water source: an appraisal. *J. Glaciol.* **12**, 207–233 (1973).
24. Ho, J. The implications of Arctic sea ice decline on shipping. *Mar. Policy* **34**, 713–715 (2010).
25. de Andrés, C. R. A., Saarinen, S. & Uuskallio, A. Review of ice challenges and ice management in port areas. *Coast. Eng. Proc.* **1**, 79 (2018).
26. Davis, S. H. *Theory of Solidification* (Cambridge Univ. Press, 2001).
27. Gupta, S. C. *The Classical Stefan Problem: Basic Concepts, Modelling and Analysis with Quasi-analytical Solutions and Methods* (Elsevier, 2017).
28. Huppert, H. E. The fluid mechanics of solidification. *J. Fluid Mech.* **212**, 209–240 (1990).
29. Bell, R. E. The role of subglacial water in ice-sheet mass balance. *Nat. Geosci.* **1**, 297–304 (2008).
30. Joughin, I., Alley, R. B. & Holland, D. M. Ice-sheet response to oceanic forcing. *Science* **338**, 1172–1176 (2012).
31. Straneo, F. & Heimbach, P. North Atlantic warming and the retreat of Greenland's outlet glaciers. *Nature* **504**, 36–43 (2013).
32. Rafat, A., Pour, H. K., Spence, C., Palmer, M. J. & MacLean, A. An analysis of ice growth and temperature dynamics in two Canadian subarctic lakes. *Cold Reg. Sci. Technol.* **210**, 103808 (2023).
33. Bodenschatz, E., Pesch, W. & Ahlers, G. Recent developments in Rayleigh–Bénard convection. *Annu. Rev. Fluid Mech.* **32**, 709–778 (2000).
34. Ahlers, G., Grossmann, S. & Lohse, D. Heat transfer and large scale dynamics in turbulent Rayleigh–Bénard convection. *Rev. Mod. Phys.* **81**, 503 (2009).
35. Lohse, D. & Xia, K. Q. Small-scale properties of turbulent Rayleigh–Bénard convection. *Annu. Rev. Fluid Mech.* **42**, 335–364 (2010).
36. Chillà, F. & Schumacher, J. New perspectives in turbulent Rayleigh–Bénard convection. *Eur. Phys. J. E* **35**, 1–25 (2012).
37. Lohse, D. & Shishkina, O. Ultimate turbulent thermal convection. *Phys. Today* **76**, 26–32 (2023).
38. Ng, C. S., Ooi, A., Lohse, D. & Chung, D. Vertical natural convection: application of the unifying theory of thermal convection. *J. Fluid Mech.* **764**, 349–361 (2015).
39. Shishkina, O. Momentum and heat transport scalings in laminar vertical convection. *Phys. Rev. E* **93**, 051102 (2016).
40. Davis, S. H., Müller, U. & Dietsche, C. Pattern selection in single-component systems coupling Bénard convection and solidification. *J. Fluid Mech.* **144**, 133–151 (1984).
41. Esfahani, B. R., Hirata, S. C., Berti, S. & Calzavarini, E. Basal melting driven by turbulent thermal convection. *Phys. Rev. Fluids* **3**, 053501 (2018).
42. Favier, B., Purseed, J. & Duchemin, L. Rayleigh–Bénard convection with a melting boundary. *J. Fluid Mech.* **858**, 437–473 (2019).
43. Satbhai, O., Roy, S., Ghosh, S., Chakraborty, S. & Lakkaraju, R. Comparison of the quasi-steady-state heat transport in phase-change and classical Rayleigh–Bénard convection for a wide range of Stefan number and Rayleigh number. *Phys. Fluids* **31**, 096605 (2019).
44. Yang, R., Howland, C. J., Liu, H. R., Verzicco, R. & Lohse, D. Morphology evolution of a melting solid layer above its melt heated from below. *J. Fluid Mech.* **956**, A23 (2023).
45. Purseed, J., Favier, B., Duchemin, L. & Hester, E. W. Bistability in Rayleigh–Bénard convection with a melting boundary. *Phys. Rev. Fluids* **5**, 023501 (2020).
46. Weady, S., Tong, J., Zidovska, A. & Ristroph, L. Anomalous convective flows carve pinnacles and scallops in melting ice. *Phys. Rev. Lett.* **128**, 044502 (2022).
47. Wang, Z., Jiang, L., Du, Y., Sun, C. & Calzavarini, E. Ice front shaping by upward convective current. *Phys. Rev. Fluids* **6**, L091501 (2021).
48. Yang, R., Chong, K. L., Liu, H. R., Verzicco, R. & Lohse, D. Abrupt transition from slow to fast melting of ice. *Phys. Rev. Fluids* **7**, 083503 (2022).
49. Wang, Z., Calzavarini, E., Sun, C. & Toschi, F. How the growth of ice depends on the fluid dynamics underneath. *Proc. Natl Acad. Sci. USA* **118**, e2012870118 (2021).
50. Wang, Z., Calzavarini, E. & Sun, C. Equilibrium states of the ice-water front in a differentially heated rectangular cell. *Europhys. Lett.* **135**, 54001 (2021).
51. Townsend, A. A. Natural convection in water over an ice surface. *Q. J. R. Meteorol. Soc.* **90**, 248–259 (1964).
52. Couston, L. A. Turbulent convection in subglacial lakes. *J. Fluid Mech.* **915**, A31 (2021).
53. Couston, L. A. et al. Topography generation by melting and freezing in a turbulent shear flow. *J. Fluid Mech.* **911**, A44 (2021).
54. Tsai, C. W., Yang, S. J. & Hwang, G. J. Maximum density effect on laminar water pipe flow solidification. *Int. J. Heat Mass Transf.* **41**, 4251–4257 (1998).
55. Du, Y., Wang, Z., Jiang, L., Calzavarini, E. & Sun, C. Sea water freezing modes in a natural convection system. *J. Fluid Mech.* **960**, A35 (2023).
56. Turner, J. S. Double-diffusive phenomena. *Annu. Rev. Fluid Mech.* **6**, 37–54 (1974).
57. Huppert, H. E. & Turner, J. S. Double-diffusive convection. *J. Fluid Mech.* **106**, 299–329 (1981).
58. Radko, T. *Double-Diffusive Convection* (Cambridge Univ. Press, 2013).
59. Garaud, P. Double-diffusive convection at low Prandtl number. *Annu. Rev. Fluid Mech.* **50**, 275–298 (2018).
60. Yang, Y., Verzicco, R., Lohse, D. & Caulfield, C. P. Layering and vertical transport in sheared double-diffusive convection in the diffusive regime. *J. Fluid Mech.* **933**, A30 (2022).
61. Peppin, S. S. L., Huppert, H. E. & Worster, M. G. Steady-state solidification of aqueous ammonium chloride. *J. Fluid Mech.* **599**, 465–476 (2008).
62. Anderson, D. M. & Guba, P. Convective phenomena in mushy layers. *Annu. Rev. Fluid Mech.* **52**, 93–119 (2020).
63. Thakur, I., Karagadde, S. & Srivastava, A. Mechanisms leading to the formation of double-diffusive layers during unidirectional solidification of aqueous NH_4Cl solution. *Phys. Rev. Fluids* **7**, 063501 (2022).
64. Rosevear, M. G., Gayen, B. & Galton-Fenzi, B. K. The role of double-diffusive convection in basal melting of Antarctic ice shelves. *Proc. Natl Acad. Sci. USA* **118**, e2007541118 (2021).
65. Mergui, S., Geoffroy, S. & Bénard, C. Ice block melting into a binary solution: coupling of the interfacial equilibrium and the flow structures. *J. Heat Transf.* **124**, 1147–1157 (2002).
66. Huppert, H. E. & Turner, J. S. On melting icebergs. *Nature* **271**, 46–48 (1978).
67. Huppert, H. E. & Turner, J. S. Ice blocks melting into a salinity gradient. *J. Fluid Mech.* **100**, 367–384 (1980).
68. Yang, R., Howland, C. J., Liu, H. R., Verzicco, R. & Lohse, D. Ice melting in salty water: layering and non-monotonic dependence on the mean salinity. *J. Fluid Mech.* **969**, R2 (2023).
69. Wilson, N. J., Vreugdenhil, C. A., Gayen, B. & Hester, E. W. Double-diffusive layer and meltwater plume effects on ice face scalloping in phase-change simulations. *Geophys. Res. Lett.* **50**, e2023GL104396 (2023).
70. Sugawara, M. & Irvine, T. F. The effect of concentration gradient on the melting of a horizontal ice plate from above. *Int. J. Heat Mass Transf.* **43**, 1591–1601 (2000).
71. Sugawara, M., Ishikura, T. & Beer, H. Effect of cavity inclination on a temperature and concentration controlled double diffusive convection at ice plate melting. *Heat Mass Transf.* **41**, 432–441 (2005).
72. Sugawara, M. et al. Visual observations of flow structure and melting front morphology in horizontal ice plate melting from above into a mixture. *Heat Mass Transf.* **43**, 1009–1018 (2007).
73. Gayen, B., Griffiths, R. W. & Kerr, R. C. Simulation of convection at a vertical ice face dissolving into saline water. *J. Fluid Mech.* **798**, 284–298 (2016).
74. Mondal, M., Gayen, B., Griffiths, R. W. & Kerr, R. C. Ablation of sloping ice faces into polar seawater. *J. Fluid Mech.* **863**, 545–571 (2019).
75. Chen, C. F. & Chen, F. Experimental study of directional solidification of aqueous ammonium chloride solution. *J. Fluid Mech.* **227**, 567–586 (1991).
76. Worster, M. G. & Wettlaufer, J. S. Natural convection, solute trapping, and channel formation during solidification of saltwater. *J. Phys. Chem. B* **101**, 6132–6136 (1997).
77. Wettlaufer, J. S., Worster, M. G. & Huppert, H. E. Natural convection during solidification of an alloy from above with application to the evolution of sea ice. *J. Fluid Mech.* **344**, 291–316 (1997).

78. Chen, C. F. Experimental study of convection in a mushy layer during directional solidification. *J. Fluid Mech.* **293**, 81–98 (1995).
79. Middleton, C. A., Thomas, C., De Wit, A. & Tison, J. L. Visualizing brine channel development and convective processes during artificial sea-ice growth using Schlieren optical methods. *J. Glaciol.* **62**, 1–17 (2016).
80. Middleton, C. A. et al. Relative role of short interfacial fingers and long internally driven streamers in convective flows below growing sea ice. *Phys. Rev. Fluids* **7**, 043503 (2022).
81. Worster, M. G. Convection in mushy layers. *Annu. Rev. Fluid Mech.* **29**, 91–122 (1997).
82. Peppin, S. S. L., Aussillous, P., Huppert, H. E. & Worster, M. G. Steady-state mushy layers: experiments and theory. *J. Fluid Mech.* **570**, 69–77 (2007).
83. Worster, M. G. & Rees Jones, D. W. Sea-ice thermodynamics and brine drainage. *Phil. Trans. R. Soc. A* **373**, 20140166 (2015).
84. Kerr, R. C., Woods, A. W., Worster, M. G. & Huppert, H. E. Solidification of an alloy cooled from above Part 1. Equilibrium growth. *J. Fluid Mech.* **216**, 323–342 (1990).
85. Kerr, R. C., Woods, A. W., Worster, M. G. & Huppert, H. E. Solidification of an alloy cooled from above Part 2. Non-equilibrium interfacial kinetics. *J. Fluid Mech.* **217**, 331–348 (1990).
86. Feltham, D. L., Untersteiner, N., Wettlaufer, J. S. & Worster, M. G. Sea ice is a mushy layer. *Geophys. Res. Lett.* **33**, L14501 (2006).
87. Wells, A. J., Hitchen, J. R. & Parkinson, J. R. G. Mushy-layer growth and convection, with application to sea ice. *Philos. Trans. A Math. Phys. Eng. Sci.* **377**, 20180165 (2019).
88. Chung, C. A. & Worster, M. G. Steady-state chimneys in a mushy layer. *J. Fluid Mech.* **455**, 387–411 (2002).
89. Ravichandran, S., Toppaladoddi, S. & Wettlaufer, J. S. The combined effects of buoyancy, rotation, and shear on phase boundary evolution. *J. Fluid Mech.* **941**, A39 (2022).
90. Toppaladoddi, S. & Wettlaufer, J. S. The combined effects of shear and buoyancy on phase boundary stability. *J. Fluid Mech.* **868**, 648–665 (2019).
91. Toppaladoddi, S. Nonlinear interactions between an unstably stratified shear flow and a phase boundary. *J. Fluid Mech.* **919**, A28 (2021).
92. Gilpin, R. R. Ice formation in a pipe containing flows in the transition and turbulent regimes. *J. Heat Transf.* **103**, 363–368 (1981).
93. Gilpin, R. R., Hirata, T. & Cheng, K. C. Wave formation and heat transfer at an ice–water interface in the presence of a turbulent flow. *J. Fluid Mech.* **99**, 619–640 (1980).
94. Bushuk, M., Holland, D. M., Stanton, T. P., Stern, A. & Gray, C. Ice scallops: a laboratory investigation of the ice–water interface. *J. Fluid Mech.* **873**, 942–976 (2019).
95. Blumberg, P. N. & Curl, R. L. Experimental and theoretical studies of dissolution roughness. *J. Fluid Mech.* **65**, 735–751 (1974).
96. Claudin, P., Durán, O. & Andreotti, B. Dissolution instability and roughening transition. *J. Fluid Mech.* **832**, R2 (2017).
97. Blass, A., Zhu, X., Verzicco, R., Lohse, D. & Stevens, R. J. A. M. Flow organization and heat transfer in turbulent wall sheared thermal convection. *J. Fluid Mech.* **897**, A22 (2020).
98. Scagliarini, A., Gylfason, Á. & Toschi, F. Heat-flux scaling in turbulent Rayleigh–Bénard convection with an imposed longitudinal wind. *Phys. Rev. E* **89**, 043012 (2014).
99. Ravichandran, S. & Wettlaufer, J. S. Melting driven by rotating Rayleigh–Bénard convection. *J. Fluid Mech.* **916**, A28 (2021).
100. Meroni, A. N., McConnochie, C. D., Cenedese, C., Sutherland, B. & Snow, K. Nonlinear influence of the Earth's rotation on iceberg melting. *J. Fluid Mech.* **858**, 832–851 (2019).
101. Kang, W. Nonsynchronous rotation of icy moon ice shells: the thermal wind perspective. *Sci. Adv.* **10**, eadk2277 (2024).
102. Hester, E. W., McConnochie, C. D., Cenedese, C., Couston, L. A. & Vasil, G. Aspect ratio affects iceberg melting. *Phys. Rev. Fluids* **6**, 023802 (2021).
103. Yang, R., Howland, C. J., Liu, H. R., Verzicco, R. & Lohse, D. Shape effect on solid melting in flowing liquid. *J. Fluid Mech.* **980**, R1 (2024).
104. FitzMaurice, A., Cenedese, C. & Straneo, F. Nonlinear response of iceberg side melting to ocean currents. *Geophys. Res. Lett.* **44**, 5637–5644 (2017).
105. Hao, Y. L. & Tao, Y. X. Melting of a solid sphere under forced and mixed convection: flow characteristics. *J. Heat Transf.* **123**, 937–950 (2001).
106. Hao, Y. L. & Tao, Y. X. Heat transfer characteristics of melting ice spheres under forced and mixed convection. *J. Heat Transf.* **124**, 891–903 (2002).
107. Moore, M. N. J. Riemann-Hilbert problems for the shapes formed by bodies dissolving, melting, and eroding in fluid flows. *Commun. Pure Appl. Math.* **70**, 1810–1831 (2017).
108. Moore, M. N. J., Ristroph, L., Childress, S., Zhang, J. & Shelley, M. J. Self-similar evolution of a body eroding in a fluid flow. *Phys. Fluids* **25**, 116602 (2013).
109. Mac Huang, J., Moore, M. N. J. & Ristroph, L. Shape dynamics and scaling laws for a body dissolving in fluid flow. *J. Fluid Mech.* **765**, R3 (2015).
110. Ristroph, L., Moore, M. N. J., Childress, S., Shelley, M. J. & Zhang, J. Sculpting of an erodible body by flowing water. *Proc. Natl Acad. Sci. USA* **109**, 19606–19609 (2012).
111. Pegler, S. S. & Davies Wykes, M. S. Shaping of melting and dissolving solids under natural convection. *J. Fluid Mech.* **900**, A35 (2020).
112. Pegler, S. S. & Davies Wykes, M. S. The convective Stefan problem: shaping under natural convection. *J. Fluid Mech.* **915**, A86 (2021).
113. Huang, J. M., Tong, J., Shelley, M. & Ristroph, L. Ultra-sharp pinnacles sculpted by natural convective dissolution. *Proc. Natl Acad. Sci. USA* **117**, 23339–23344 (2020).
114. Machicoane, N., Bonaventure, J. & Volk, R. Melting dynamics of large ice balls in a turbulent swirling flow. *Phys. Fluids* **25**, 125101 (2013).
115. Manucharyan, G. E. & Montemuro, B. P. SubZero: a sea ice model with an explicit representation of the floe life cycle. *J. Adv. Model. Earth Syst.* **14**, e2022MS003247 (2022).
116. Marshall, S. *The Cryosphere* Vol. 4 (Princeton Univ. Press, 2011).
117. Golden, K. M. et al. Modeling sea ice. *Not. Am. Math. Soc.* **67**, 1535–1555 (2020).
118. Fetterer, F. & Untersteiner, N. Observations of melt ponds on Arctic sea ice. *J. Geophys. Res. Oceans* **103**, 24821–24835 (1998).
119. Flocco, D., Schroeder, D., Feltham, D. L. & Hunke, E. C. Impact of melt ponds on Arctic sea ice simulations from 1990 to 2007. *J. Geophys. Res. Oceans* **117**, C09032 (2012).
120. Schröder, D., Feltham, D., Flocco, D. & Tsamados, M. September Arctic sea-ice minimum predicted by spring melt-pond fraction. *Nat. Clim. Change* **4**, 353–357 (2014).
121. Skyllingstad, E. D., Paulson, C. A. & Perovich, D. K. Simulation of melt pond evolution on level ice. *J. Geophys. Res. Oceans* **114**, C12019 (2009).
122. Flocco, D. & Feltham, D. L. A continuum model of melt pond evolution on Arctic sea ice. *J. Geophys. Res. Oceans* **112**, C08016 (2007).
123. Flocco, D., Feltham, D. L., Bailey, E. & Schroeder, D. The refreezing of melt ponds on Arctic sea ice. *J. Geophys. Res. Oceans* **120**, 647–659 (2015).
124. Yang, R., Howland, C. J., Liu, H. R., Verzicco, R. & Lohse, D. Bistability in radiatively heated melt ponds. *Phys. Rev. Lett.* **131**, 234002 (2023).
125. Skyllingstad, E. D. & Paulson, C. A. A numerical study of melt ponds. *J. Geophys. Res. Oceans* **112**, C08015 (2007).
126. Scagliarini, A., Calzavarini, E., Mansutti, D. & Toschi, F. in *Mathematical Approach to Climate Change and its Impacts* (eds Cannarsa, P. et al.) 179–198 (Springer, 2020).
127. Polashenski, C., Perovich, D. & Courville, Z. The mechanisms of sea ice melt pond formation and evolution. *J. Geophys. Res. Oceans* **117**, C01001 (2012).
128. Smith, M. M. et al. Quantifying false bottoms and under-ice meltwater layers beneath Arctic summer sea ice with fine-scale observations. *Elem. Sci. Anth.* **10**, 000116 (2022).
129. Martin, S. & Kauffman, P. The evolution of under-ice melt ponds, or double diffusion at the freezing point. *J. Fluid Mech.* **64**, 507–528 (1974).
130. Provost, C., Sennéchael, N. & Sirven, J. Contrasted summer processes in the sea ice for two neighboring floes north of 84°N: surface and basal melt and false bottom formation. *J. Geophys. Res. Oceans* **124**, 3963–3986 (2019).
131. Notz, D. et al. Impact of underwater-ice evolution on Arctic summer sea ice. *J. Geophys. Res. Oceans* **108**, 3223 (2003).
132. Stevens, C. et al. Ocean mixing and heat transport processes observed under the Ross Ice Shelf control its basal melting. *Proc. Natl Acad. Sci. USA* **117**, 16799–16804 (2020).
133. Notz, D. & Worster, M. G. In situ measurements of the evolution of young sea ice. *J. Geophys. Res. Oceans* **113**, C03001 (2008).
134. Notz, D. & Worster, M. G. Desalination processes of sea ice revisited. *J. Geophys. Res. Oceans* **114**, C05006 (2009).
135. Griewank, P. J. & Notz, D. Insights into brine dynamics and sea ice desalination from a 1-D model study of gravity drainage. *J. Geophys. Res. Oceans* **118**, 3370–3386 (2013).
136. Jardon, F. P. et al. Full-depth desalination of warm sea ice. *J. Geophy. Res. Oceans* **118**, 435–447 (2013).
137. Washam, P. et al. Direct observations of melting, freezing, and ocean circulation in an ice shelf basal crevasse. *Sci. Adv.* **9**, eadi7638 (2023).
138. Ristroph, L. Sculpting with flow. *J. Fluid Mech.* **838**, 1–4 (2018).
139. Meakin, P. & Jamtveit, B. Geological pattern formation by growth and dissolution in aqueous systems. *Proc. R. Soc. A* **466**, 659–694 (2010).
140. Kämäri, M., Alho, P., Colpaert, A. & Lotsari, E. Spatial variation of river-ice thickness in a meandering river. *Cold Reg. Sci. Technol.* **137**, 17–29 (2017).
141. Cenedese, C. & Straneo, F. Icebergs melting. *Annu. Rev. Fluid Mech.* **55**, 377–402 (2023).
142. Rampal, P., Weiss, J., Marsan, D. & Bourgoin, M. Arctic sea ice velocity field: general circulation and turbulent-like fluctuations. *J. Geophys. Res. Oceans* **114**, C10014 (2009).
143. Manucharyan, G. E., Lopez-Acosta, R. & Wilhelmus, M. M. Spinning ice floes reveal intensification of mesoscale eddies in the western Arctic Ocean. *Sci. Rep.* **12**, 7070 (2022).
144. Wengrove, M. E., Pettit, E. C., Nash, J. D., Jackson, R. H. & Skyllingstad, E. D. Melting of glacier ice enhanced by bursting air bubbles. *Nat. Geosci.* **16**, 871–876 (2023).
145. Rampal, P., Bouillon, S., Ólason, E. & Morlighem, M. neXtSIM: a new Lagrangian sea ice model. *Cryosphere* **10**, 1055–1073 (2016).
146. Dolatshah, A., Bennetts, L. G., Meylan, M. H., Monty, J. P. & Toffoli, A. An experimental model of wind-induced rafting of pancake ice floating on waves. In *34th International Workshop on Water Waves and Floating Bodies* (IWWWFB, 2019).
147. Dolatshah, A. et al. Hydroelastic interactions between water waves and floating freshwater ice. *Phys. Fluids* **30**, 091702 (2018).
148. Naumann, A. K., Notz, D., Håvik, L. & Sirevaag, A. Laboratory study of initial sea-ice growth: properties of grease ice and nilas. *Cryosphere* **6**, 729–741 (2012).
149. Fichefet, T. & Gaspar, P. A model study of upper ocean-sea ice interactions. *J. Phys. Oceanogr.* **18**, 181–195 (1988).
150. Fichefet, T. & Maqueda, M. A. M. Sensitivity of a global sea ice model to the treatment of ice thermodynamics and dynamics. *J. Geophys. Res. Oceans* **102**, 12609–12646 (1997).
151. Goosse, H. & Fichefet, T. Importance of ice-ocean interactions for the global ocean circulation: a model study. *J. Geophys. Res. Oceans* **104**, 23337–23355 (1999).
152. Martin, T. & Adcroft, A. Parameterizing the fresh-water flux from land ice to ocean with interactive icebergs in a coupled climate model. *Ocean Model.* **34**, 111–124 (2010).
153. Rae, J. G. L. et al. Development of the Global Sea Ice 6.0 CICE configuration for the Met Office Global Coupled Model. *Geosci. Model Dev.* **8**, 2221–2230 (2015).
154. Rousset, C. et al. The Louvain-La-Neuve sea ice model LIM3.6: global and regional capabilities. *Geosci. Model Dev.* **8**, 2991–3005 (2015).

155. Notz, D. et al. The CMIP6 Sea-Ice Model Intercomparison Project (SIMIP): understanding sea ice through climate-model simulations. *Geosci. Model Dev.* **9**, 3427–3446 (2016).
156. Notz, D. & Community, S. Arctic sea ice in CMIP6. *Geophys. Res. Lett.* **47**, e2019GL086749 (2020).
157. Pelletier, C. et al. PARASO, a circum-Antarctic fully coupled ice-sheet–ocean–sea-ice–atmosphere–land model involving f.ETISh1.7, NEMO3.6, LIM3.6, COSMO5.0 and CLM4.5. *Geosci. Model Dev.* **15**, 553–594 (2022).
158. Diamond, R., Schroeder, D., Sime, L. C., Ridley, J. & Feltham, D. The significance of the melt-pond scheme in a CMIP6 global climate model. *J. Clim.* **37**, 249–268 (2023).
159. Hunke, E. C., Notz, D., Turner, A. K. & Vancoppenolle, M. The multiphase physics of sea ice: a review for model developers. *Cryosphere* **5**, 989–1009 (2011).
160. Tsamados, M. et al. Impact of variable atmospheric and oceanic form drag on simulations of Arctic sea ice. *J. Phys. Oceanogr.* **44**, 1329–1353 (2014).
161. Ezhova, E., Cenedese, C. & Brandt, L. Dynamics of three-dimensional turbulent wall plumes and implications for estimates of submarine glacier melting. *J. Phys. Oceanogr.* **48**, 1941–1950 (2018).
162. Hewitt, I. J. Subglacial plumes. *Annu. Rev. Fluid Mech.* **52**, 145–169 (2020).
163. Patmore, R. D., Holland, P. R., Vreugdenhil, C. A., Jenkins, A. & Taylor, J. R. Turbulence in the ice shelf–ocean boundary current and its sensitivity to model resolution. *J. Phys. Oceanogr.* **53**, 613–633 (2023).
164. Guarino, M. V. et al. Sea-ice-free Arctic during the last interglacial supports fast future loss. *Nat. Clim. Change* **10**, 928–932 (2020).
165. Miao, X., Xie, H., Ackley, S. F., Perovich, D. K. & Ke, C. Object-based detection of Arctic sea ice and melt ponds using high spatial resolution aerial photographs. *Cold Reg. Sci. Technol.* **119**, 211–222 (2015).
166. Hobson, B. W., Sherman, A. D. & McGill, P. R. Imaging and sampling beneath free-drifting icebergs with a remotely operated vehicle. *Deep Sea Res. 2 Top. Stud. Oceanogr.* **58**, 1311–1317 (2011).

Acknowledgements
The authors thank D. Lohse, F. Toschi, R. Verzicco, S. G. Huisman, Y. Yang, Z. Wang, R. Yang, L. Jiang, R. Volk, M. Bougoin, S. Hirata, S. Berti and A. Scagliarini for discussions on this topic over the years. The work has been supported by the Natural Science Foundation of China under grant no. 11988102, and the New Cornerstone Science Foundation through the New Cornerstone Investigator Program and the XPLORER Prize.

Author contributions
All authors contributed to all aspects of the manuscript.

Competing interests
The authors declare no competing interests.

Additional information

Peer review information *Nature Reviews Physics* thanks Nicholas Moore and the other, anonymous, reviewer(s) for their contribution to the peer review of this work.